Rare earth elements in the North Atlantic, part II: Partition coefficients

Marion Lagarde, Viet Quoc Pham, Nolwenn Lemaitre, Moustafa Belhadj, Catherine Jeandel

To cite this version:

Rare earth elements in the North Atlantic, part II: Partition coefficients

Marion Lagarde [a,b,*], Viet Quoc Pham [b,c], Nolwenn Lemaitre [b], Moustafa Belhadj [b], Catherine Jeandel [b]

[a] *LOCEAN-IPSL, Sorbonne Université/IRD/CNRS/MNHN, Paris, France*
[b] *LEGOS, CNRS, UT3, CNES, IRD, University of Toulouse, 14 avenue Edouard Belin, Toulouse 31400, France*
[c] *Institute of Environmental Technology, 18 Hoàng Quốc Việt street, Cầu Giấy, Hanoi, Viet Nam*

ABSTRACT

This study presents the first basin scale section of the partition coefficients (Kd) of 14 rare earth elements (REE) along the GEOVIDE (GEOTRACES GA01 cruise) transect, in the subpolar North Atlantic (May–June 2014, R/V Pourquoi Pas?). Although Kd data are very scarce in the literature, it is a key parameter of element cycle modeling, controlling the scavenging efficiency by particles. Because of this lack of data, Kd are generally adjusted in the models to obtain the best agreement between modeled and observed concentrations. This shortcoming likely contributes to make the modeling of the oceanic REE cycles challenging. This is well illustrated by the difficulty to satisfactorily simulate both Nd concentrations and isotopic compositions.

Here, we determined Kd(REE) at 10 stations, calculated from previously published dissolved and particulate REE concentrations, and from suspended particulate matter (SPM) concentrations. The data required for the calculation of SPM concentrations were obtained in the framework of the GEOVIDE cruise. Kd profiles displayed minimum values at the surface, variations in the upper 400 m, and an increase with depth below 400 m. The expression of the ratio of particulate to dissolved REE concentrations as a function of SPM concentrations showed that manganese oxides (MnO_2) were the main driver of REE scavenging, followed by the lithogenic phase and iron hydroxides ($Fe(OH)_3$). Our study also highlighted that REE scavenging preferentially depended on the relative proportion of these three phases rather than on their absolute concentrations. These conclusions were evaluated by a Pearson correlation test, with correlation coefficients of 0.83, 0.84, and 0.75 between Kd(Nd) and the MnO_2, lithogenic, and $Fe(OH)_3$ fractions, respectively.

Finally, we proposed two Kd(Nd) parameterizations as a function of the particulate phase fractions. The first parameterization included MnO_2 and $Fe(OH)_3$, phases that are currently not represented in Nd cycle models, and showed a good agreement between observed and calculated Kd(Nd) ($R^2 = 0.84$, $p < 0.05$). The second parameterization did not include the MnO_2 and $Fe(OH)_3$ phases, as in existing Nd cycle models, leading to a lower correlation between observed and calculated Kd(Nd) ($R^2 = 0.71$, $p < 0.05$). Given that scavenging is an important process in the water column, these results reveal a bias in Nd cycle (and more generally in REE cycles) with models. Determining these Kd values is promising and therefore recommended in the future for improving Nd (and REE) cycle models and our Nd (REE) cycle understanding.

1. Introduction

The biogeochemical oceanic cycle of an element depends on its sources, sinks and internal cycle in the water column (uptake and removal at the surface, regeneration at depth, transport by the currents, (SCOR, 2007). The sources include riverine inputs, atmospheric deposits, hydrothermal vents, submarine groundwater discharges, and the diffusion and dissolution of sediment deposited on margins and the seafloor (Duce et al., 1991; Moore, 1996; Lacan and Jeandel, 2001; Bruland and Lohan, 2003; Burnett et al., 2006; Planquette et al., 2007; Arsouze et al., 2009; Libes, 2009; Moore et al., 2013; Labatut et al., 2014; Jeandel and Oelkers, 2015; Jickells et al., 2016; Deng et al., 2017). The importance of these sources varies from one element to another (Libes, 2009), both for the dissolved and particulate forms, and the ratio

---

between these two forms is also element dependent (Jeandel and Oelkers, 2015). Sources control the intensity of primary production and thus the transfer of atmospheric carbon to organic matter via photosynthesis. Indeed, they determine the availability of the macro- and micronutrients required for the development of photosynthetic organisms (de Baar et al., 2005; Bruland and Lohan, 2006; Boyd et al., 2007; SCOR, 2007; Pollard et al., 2007). The elements contained in the particles, from carbon to trace metals, are then transferred to the ocean floor, where they are sequestered. This mechanism is named the biological pump (Sarmiento and Gruber, 2006). While sinking, the particles undergo further transformations: remineralization, adsorption or desorption of chemical elements or complexes, aggregation and disaggregation. These processes of dissolved-particulate exchanges (DPE) affect particle composition and, therefore, the vertical transfer of elements (Jeandel and Oelkers, 2015; Lam and Marchal, 2015 and references therein) as well as their oceanic residence time (Lal, 1977; Turekian, 1977). It is therefore essential to understand and quantify these exchanges at all scales, which is one of the objectives of the international GEOTRACES program (SCOR, 2007; Anderson and Henderson, 2015).

Element reactivity is the main driver of DPE. Reactivity of most of the bioactive elements (e.g., macronutrients such as N, Si, P) is controlled by surface biological uptake followed by remineralization at depth, leading to "nutrient shape vertical profiles" (Roy-Barman and Jeandel, 2016). Bioactive trace metals (also called micronutrients, such as Fe, Zn, Cu, Co, Ni or Mn) display a variable solubility depending on the occurrence of biological activity and/or presence of complexing agents, redox conditions, or authigenic precipitation (Tagliabue et al., 2023). The shape of their profiles results from their stabilization in the dissolved phase on one hand, i.e. from the various complexes and ligands maintaining these elements in solution, and from the biological uptake and their affinity for other types of particles such as lithogenic particles on the other hand (Goldberg, 1954; Turekian, 1977; Bruland and Lohan, 2003; Jeandel et al., 2015; Lam et al., 2015; Tagliabue et al., 2023). For non-bioactive elements, the main driver of DPE is the competition between complexation processes in solution and at the surface of particles (Byrne and Kim, 1990). Thus, the nature and abundance of particles are also key factors of DPE (Anderson, 2003; Roy-Barman et al., 2005; Akagi et al., 2011).

Any element affinity for particles is defined as the ratio of its concentration in the labile particulate phase to its concentration in the dissolved phase. However, it is not always possible to determine the labile concentration; thus, the total particulate concentration is often considered instead. The ratio of an element concentration in the particulate phase (expressed per unit of mass of solid, Eq. 4) to its concentration in the dissolved phase (expressed per unit of mass of liquid, Eq. 3) is called the partition coefficient, or Kd (Chase et al., 2002, p.200; Siddall et al., 2008; Garcia-Solsona et al., 2014; Jeandel et al., 2015; Stichel et al., 2020; Basak et al., 2024). Since the mass of filtered particles is also rarely known, oceanographers are constrained to use the ratio of particulate to dissolved concentration per kg of seawater. This ratio is Kd' (Sholkovitz et al., 1994; Jeandel et al., 1995; Garcia-Solsona et al., 2014). The limit of Kd' is that it does not consider the stock effect induced by the particulate pool. In other words, a high Kd' can reflect either significant scavenging driven by a few particles, or lower scavenging driven by a higher concentrations of suspended particulate matter (SPM).

Because of the lack of Kd data, the models simulating oceanic trace element distributions often parameterize Kd to generate dissolved concentrations that most closely approximate observations (Siddall et al., 2008; Arsouze et al., 2009; Rempfer et al., 2011; Pöppelmeier et al., 2022; Pasquier et al., 2022; Ayache et al., 2023). These Kd are adjusted for each constituent phase of the particles, and are considered as constant over the model study area. In reality, their observed distributions are spatially highly variable, as shown for Pa and Th but also for rare earth elements (REE) (Anderson et al., 1983; Jeandel et al., 1995;

Tachikawa et al., 1999b; Roy-Barman et al., 2005, 2009; Garcia-Solsona et al., 2014). Yet, scarce data availability does not allow the inclusion of this variability in the models.

Among the trace elements, the REE family is a suitable tracer of DPE. They are tracers of lithogenic inputs (Sholkovitz et al., 1999; Tachikawa et al., 1999a; Grenier et al., 2018; Lagarde et al., 2020) because of their crustal abundance relative to their oceanic concentrations, as well as their lack of biological function, which prevents their subtraction by primary producers other than methanotrophs (Shiller et al., 2017; Bayon et al., 2020; Meyer et al., 2021). In the ocean, the proportion of REE being in the form of free cations gradually decrease along the REE series (Schijf et al., 2015), resulting in lightest REE (LREE, from lanthanum (La) to gadolinium (Gd); atomic numbers 57–64) being more easily scavenged by particles than the heaviest REE (HREE, from terbium (Tb) to lutetium (Lu); atomic numbers 65–71) (Byrne and Kim, 1990). Together with the particular reactivity of Ce (the second REE of the series), the balance between LREE and HREE thus provides information on the ability of particles to remove trace elements from the dissolved phase, mainly via oxides and hydroxides (Palmer and Elderfield, 1986; Bau et al., 1996; Bau and Koschinsky, 2009; Ohta and Kawabe, 2001). Among LREE, Ce can be oxidized biotically or abiotically into Ce(IV), an oxidation state that other REE do not display. As Ce(IV) is insoluble, the intensity of Ce subtraction in the dissolved phase relative to other REE provides information on their adsorption/desorption cycles. (Elderfield, 1988; Moffett, 1990, 1994; Byrne and Kim, 1990; Bau and Dulski, 1996; Tachikawa et al., 1999a).

In this study, we investigated REE partition coefficients in the subpolar North Atlantic. Samples were collected during the GEOVIDE cruise (GEOTRACES GA01, May–June 2014, R/V Pourquoi Pas?). The cruise aimed to achieve a comprehensive documentation of the distributions of trace elements and their isotopes in the subpolar North Atlantic, in both the dissolved and particulate phases (Sarthou et al., 2018). During the cruise, a joint effort was made to collect samples for analysis of the dominant particulate phases and the various dissolved and particulate trace elements at the same depths, allowing the calculation of particle mass and partition coefficients. The various biogeochemical provinces crossed along this trans-Atlantic transect also allowed the characterization of particles of very distinct origins: mainly lithogenic at the Iberian margin and on the Greenland shelf, from a strong coccolithophorid bloom in the Icelandic basin, and from a declining diatom bloom in the Labrador and Irminger Seas (Lemaitre et al., 2018).

This study is structured as follows. In a first part, the previously published particulate (Lagarde et al., 2020) and dissolved (Part 1 of this work, Lagarde et al., 2024) REE concentrations are combined and compared to the SPM concentrations to determine to which extent the partition between the dissolved and particulate phases depends on the particle load, and if it varies along the section. Secondly, the coefficients Kd and Kd' are established along the section for all REE, with and without a lithogenic correction. The need for a lithogenic correction is discussed in the light of the results. The relative effect of the different major particulate fractions on Kd is then investigated through a Pearson correlation test, to determine the role of Mn oxides an Fe hydroxides, major actors of REE scavenging. The possibility to parametrize Kd as a function of the particle composition is explored from there. Finally, this parametrization is used to compare the Kd associated to each of the major particulate phases to those used in models (Siddall et al., 2008; Arsouze et al., 2009; Rempfer et al., 2011; Gu et al., 2017).

2. Material and methods

The partition coefficients (Kd) presented in this study were established at ten stations along the GEOVIDE transect, between the surface and 1500 m, the highest resolution to date for this parameter. The GEOVIDE cruise (May–June 2014, R/V "Pourquoi Pas?") is presented in detail in Sarthou et al. (2018) and shortly described in the companion paper (Lagarde et al., 2024, Part I). Thus, the following presentation of

the cruise focuses on the elements of interest for DPE.

2.1. Study area: The subpolar North Atlantic

The GEOVIDE cruise started in Lisbon, Portugal, and headed to the southern tip of Greenland, before continuing to Newfoundland (Fig. 1). The circulation in the area is summarized in Fig. 1 and described in the companion paper (Lagarde et al., 2024, Part I), based on the works of García-Ibáñez et al. (2015, 2018) and Zunino et al. (2017).

The GEOVIDE cruise crossed three distinct biogeochemical provinces (Longhurst, 1995; Lemaitre et al., 2018) (colored boxes in Fig. 1). The first region comprised stations 1, 13 and 17 (orange box in Fig. 1). It was under the influence of the Iberian margin, a source of significant particulate inputs of iron, manganese and REE, particularly pronounced in the nepheloid layers (Gourain et al., 2019; Lagarde et al., 2020; Lagarde et al., 2024, Part I of this study).

The second region (green box in Fig. 1) encompasses the West European and Icelandic basins, which included stations 21, 26, 32, and 38, the latter being above the Reykjanes Ridge. It was characterized by a stronger primary production, observed during the cruise, and dominated by coccolithophorids (Lemaitre et al., 2018; Fonseca-Batista et al., 2019).

The third region (blue box in Fig. 1) includes the Irminger and Labrador Seas where stations 44, 51, 64 and 69 were located. A bloom of diatoms was at its maximum in this area ca 50 days before the cruise in the Irminger Sea and the Labrador Sea. Station 53, located on the continental shelf at the southern end of Greenland, was marked by strong lithogenic inputs. Station 77 also reflected the influence of the Newfoundland margin, with a more pronounced lithogenic fraction than the other Labrador Sea stations. These inputs were weaker than at the Iberian margin, but also more homogeneous, with no pronounced nepheloid layers (Gourain et al., 2019; Lagarde et al., 2020).

2.2. Particulate and dissolved REE concentrations

2.2.1. Particulate REE

The collection, chemistry and measurement of particulate samples were described in detail in Lagarde et al. (2020). The particles were totally digested; thus, the pREE concentrations were not measured in the labile phase. Based on the distribution of ^{232}Th, a lithogenic conservative tracer, Lagarde et al. (2020) showed 1) strong lithogenic inputs at the Iberian margin, with maximum values in the intermediate nepheloid layers (INL); 2) freshly formed biogenic particles in the Iceland basin; and 3) a stronger particle affinity for HREEs than for LREEs in areas of high biogenic silica concentration (i.e., Irminger and Labrador seas), in contradiction with previously published studies (Sutorius et al., 2022) but consistent with the hypotheses of Akagi et al. (2011).

2.2.2. Dissolved REE

Dissolved sample collection and analysis along with results are presented in Lagarde et al. (2024, Part I). This study shows that the lithogenic particulate inputs are at the origin of dissolved REE (dREE) enrichment due to particle dissolution. In the Irminger and Labrador Seas, the REE subtraction linked to the diatom bloom was compensated by external inputs. Below 1500 m, strong scavenging explains the dREE concentration decrease with depth all along the section.

2.3. Calculation of suspended particulate matter concentrations

Following Lam et al. (2015b), the mass of the major phases in the suspended particles was calculated. These include organic matter, lithogenic material, inorganic opal and calcium carbonate (phytoplanktonic tests), Mn oxides and Fe hydroxides. The mass of organic matter was calculated from the concentration of particulate organic carbon (POC) and that of lithogenic material based on the concentrations of particulate Al. The opal mass was calculated from the biogenic
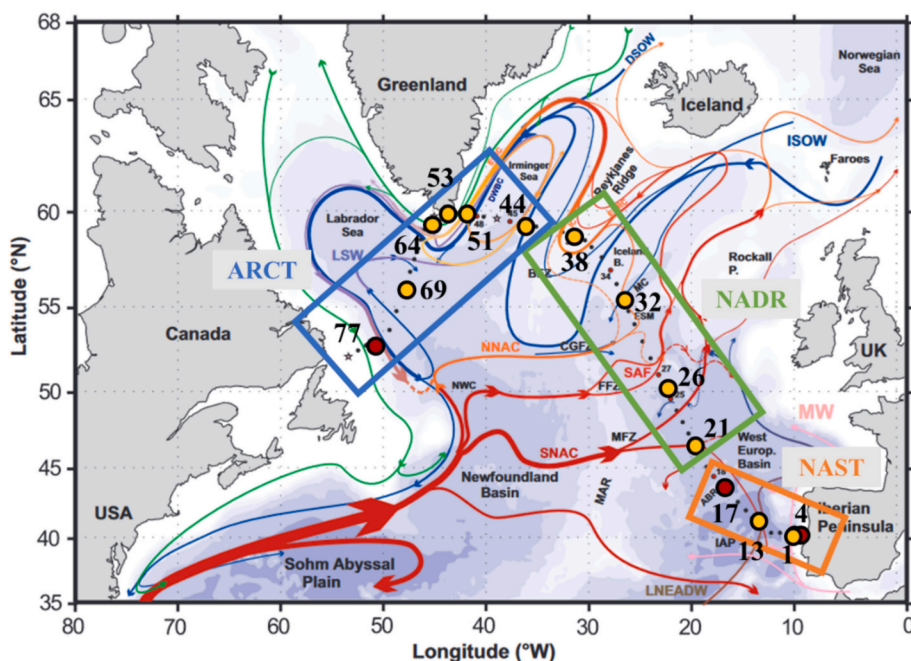
Fig. 1. Map of the studied area (Subpolar North Atlantic, SPNA), including schematized circulation features, adapted from Zunino et al. (2017). Bathymetry colour changes at 100 m, 1000 m, and every 1000 m below 1000 m. Red and green arrows represent the main surface currents; pink and orange arrows represent currents at intermediate depths; blue and purple arrows represent the deep currents. The dots represent the GEOVIDE section. The red dots correspond to stations where the suspended particulate matter concentration (SPM) was calculated, and the yellow dots are stations where both partition coefficients and the SPM concentration were calculated. The boxes delimit the main biogeochemical provinces of the are: the North Atlantic subtropical Zone (NAST, orange box), the North Atlantic Drift Region (NADR, green box) and the Arctic region (ARCT, blue box). (For interpretation of the references to colour in this figure legend, the reader is referred to the web version of this article.)

silica concentration, and the calcium carbonate mass from the calcium concentration (measured in the same samples as for pREE analysis; Lemaitre et al., 2018; Lagarde et al., 2020). The Fe hydroxide and Mn oxide concentrations were calculated from the particulate Fe and Mn concentrations respectively (Gourain et al., 2019). The sum of all these masses gives the suspended particulate matter concentration at a given point (Eq. 1). The relative contribution of each phase to the SPM is deduced from Eq. (2).

$$SPM \left[\mu g.L^{-1} \right] = [CaCO3] + [litho] + [Fe(OH)_3] + [MNO_2] + [SiO_2] + [POM] \tag{1}$$

$$\%CaCO3 + \%litho + \%(Fe(OH))_3 + \%(MnO)_2 + \%(SiO)_2 + \%POM = 100\% \tag{2}$$

Above 200 m, all element concentrations required for the calculations were available at all stations discussed in this work, allowing a relatively accurate estimation of Kd. From 200 m to 1500 m, BSi and POC were not measured. At 200 m, POM was still accounting for ~75% of the SPM, and the contribution of opal varied from 1% to 24%, which is not negligible (Fig. S1). Thus, opal and POM masses were extrapolated from 200 m to 1500 m, based on the attenuation of their concentrations observed by Marsay et al. (2015) in the same area. The details of this extrapolation are presented in Appendix 1.

The SPM concentrations are presented in Fig. 2, and the concentrations of each fraction are reported in Table S1. They vary from ~15 μg. L^{-1} to 1700 μg.L^{-1}. In the upper 200 m, the high SPM (>250 μg.L^{-1}) values are consistent with the high productivity observed in these layers (Fonseca-Batista et al., 2019; Lemaitre et al., 2018; Sanders et al., 2014). These results are also comparable with SPM concentrations previously measured in the same area (McCave and Hall, 2002, 70–300 μg.L^{-1}; Lal, 1977, > 300 μg.L^{-1} at the surface). Surface SPM values are generally higher in the Irminger and Labrador Seas than east of the section, reflecting opal contribution from the diatom bloom in the ARCT region.

Below the surface, high SPM concentrations are observed at station 1 (150 m, 250 m and 500 m), and at stations 13 and 21 at 250 m. Along the Iberian margin, SPM values ranging between 400 μg.L^{-1} and 600 μg.L^{-1} are also consistent with the strong lithogenic inputs observed off the Portugal coast (Lagarde et al., 2020). The relative contributions of the various phases to the SPM stocks at each depth are presented in the supplementary material (Fig. S1). Station 38 is characterized by higher

SPM values than its neighboring stations down to 1500 m. This is due to higher PCa contents, reaching 14 μmol.L^{-1} at some depths while not exceeding 1 μmol.L^{-1} at the other stations. A declining bloom of coccolithophorids occurred in this area at the time of the cruise, which was more pronounced above the Reykjanes ridge (corresponding to station 38) than at other stations of the Iceland basin; this was consistent with a significant proportion of haptophytes in the phytoplankton (Tonnard, 2018; Lemaitre et al., 2018). In addition, station 38 is circumvented by the East Reykjanes Ridge Current that becomes the Irminger Current, isolating the Subpolar Mode Water. Both its specific biogeochemistry and aforementioned dynamics make this station disconnected from the other stations of the Iceland basin and could explain the high PCa values.

3. Results

3.1. Particulate to dissolved concentration ratios in seawater: Kd'

The REE repartition between the particulate and dissolved phases is expressed with Kd' (Eq. 3), which represents the ratio of the pREE concentrations per liter of seawater onto the dREE concentrations:

$$Kd' = [pREE]/[dREE] \tag{3}$$

Kd' decreases along the REE series, as REE solubility increases (Schijf et al., 2015). Kd' values of this study are presented in Fig. 3 for Ce, Nd and Yb. Kd' reflects the influence of the sediment inputs at the Iberian margin, with >10% of Nd and >2.5% of Yb being contained in the particulate phase in the nepheloid layers at 250 m, 500 m and 1000 m. In the Iceland basin, these proportions decrease sharply, with <5% of Nd and 1% of Yb in the particulate phase. The Irminger and Labrador Seas contrast with the Iceland basin and are similar to the Iberian margin, with >10% of Nd and >2.5% of Yb being in the particulate phase. Lithogenic inputs contribute to these relatively high proportions at stations 51, 77 and in a lesser extent at station 69. Far from any lithogenic inputs, Kd' display values consistent with preceding observations, i.e. 2.5%–4% of LREE and 1%–2% of HREE contained in particles in the Atlantic Ocean (Sholkovitz et al., 1994; Jeandel et al., 1998; Garcia-Solsona et al., 2014). Contrastingly with other REE, the Ce proportion contained in particles tends to be higher in the eastern part of the section (Fig. 3).
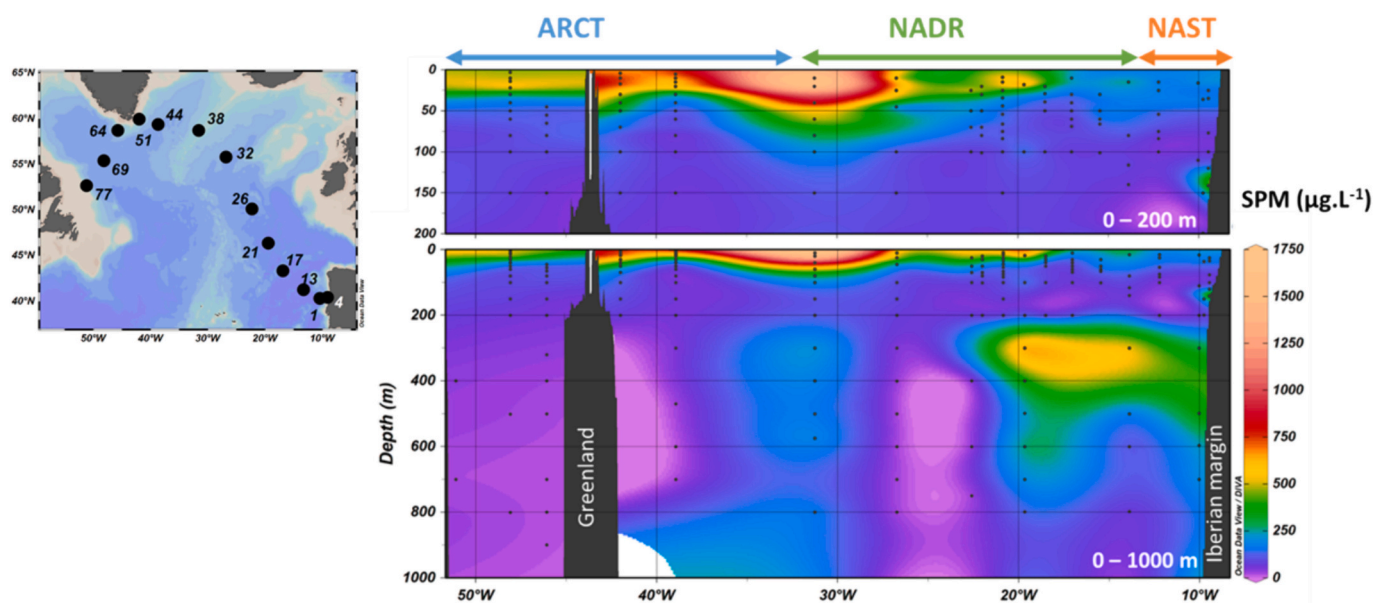

Fig. 2. Calculated suspended particulate matter concentrations (SPM) at GEOVIDE stations located on the map, with a focus on the upper 200 m in the upper panel. Interpolated and plotted with Ocean Data View (Schlitzer, 2023).
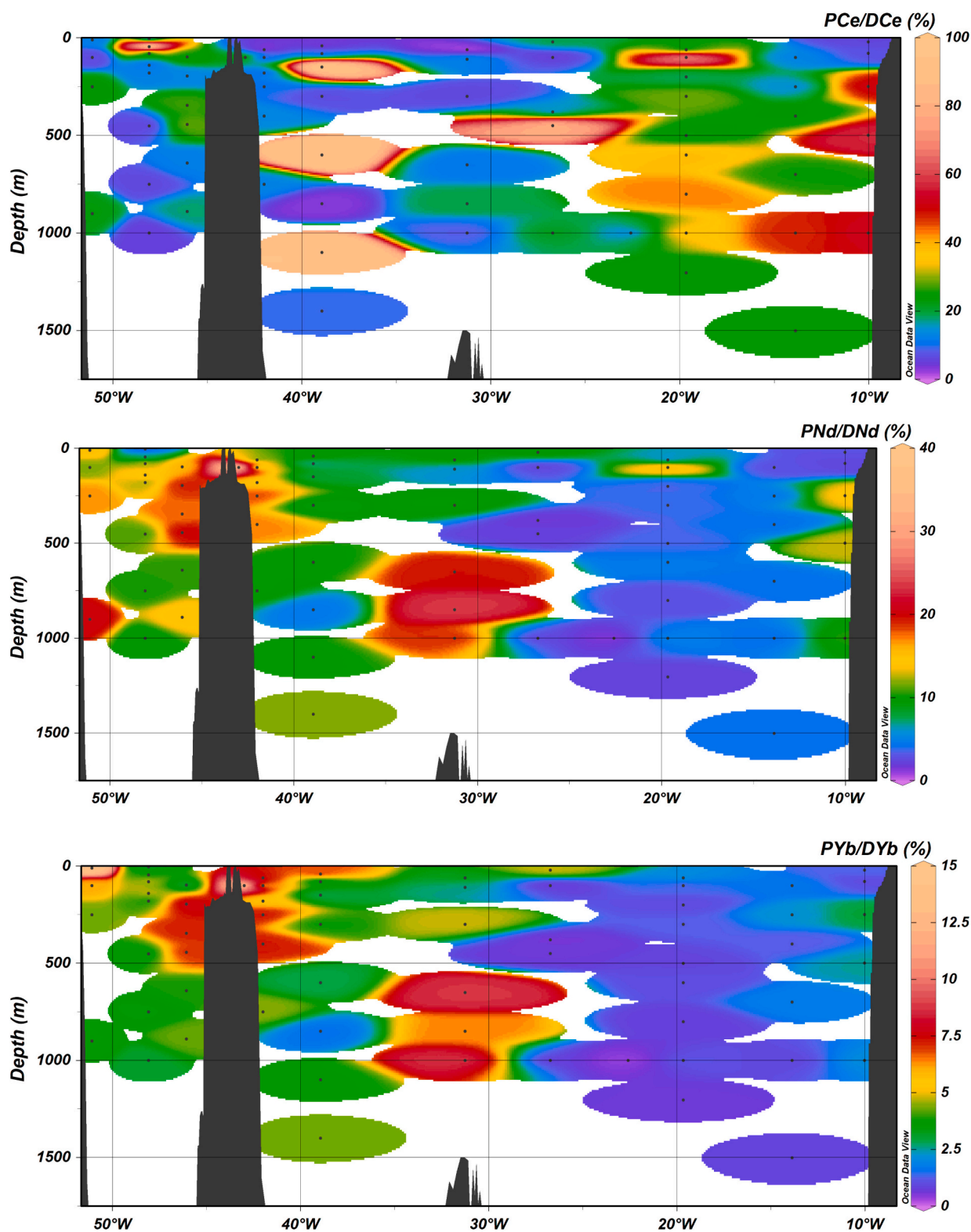
Fig. 3. Kd' values (particulate to dissolved concentration ratios) for Ce, Nd and Yb, in percentage. Interpolated and plotted with Ocean Data View (Schlitzer, 2023).

3.2. Partition coefficient Kd

The Kd is defined in eq. (4). Kd can either be dimensionless, as in this study, or expressed in g.g^{-1}.

$$K_d = \frac{[PREE]}{[DREE]*SPM} \tag{4}$$

Kd profiles of Ce, Nd and Yb are presented in Fig. 4. Kd values of all investigated REE are reported in Table S2 (Appendix 2). The only published Kd data set in the North Atlantic is compared to this study in Appendix 2 (Fig. S2; Stichel et al., 2020). A direct comparison with our results is possible at one of their 5 sampling sites only, between the GEOVIDE GA01 station 44 and their nearby GEOTRACES GA02 station 6 in the Irminger Sea. Both SPM and Kd(Nd) are in very good agreement at
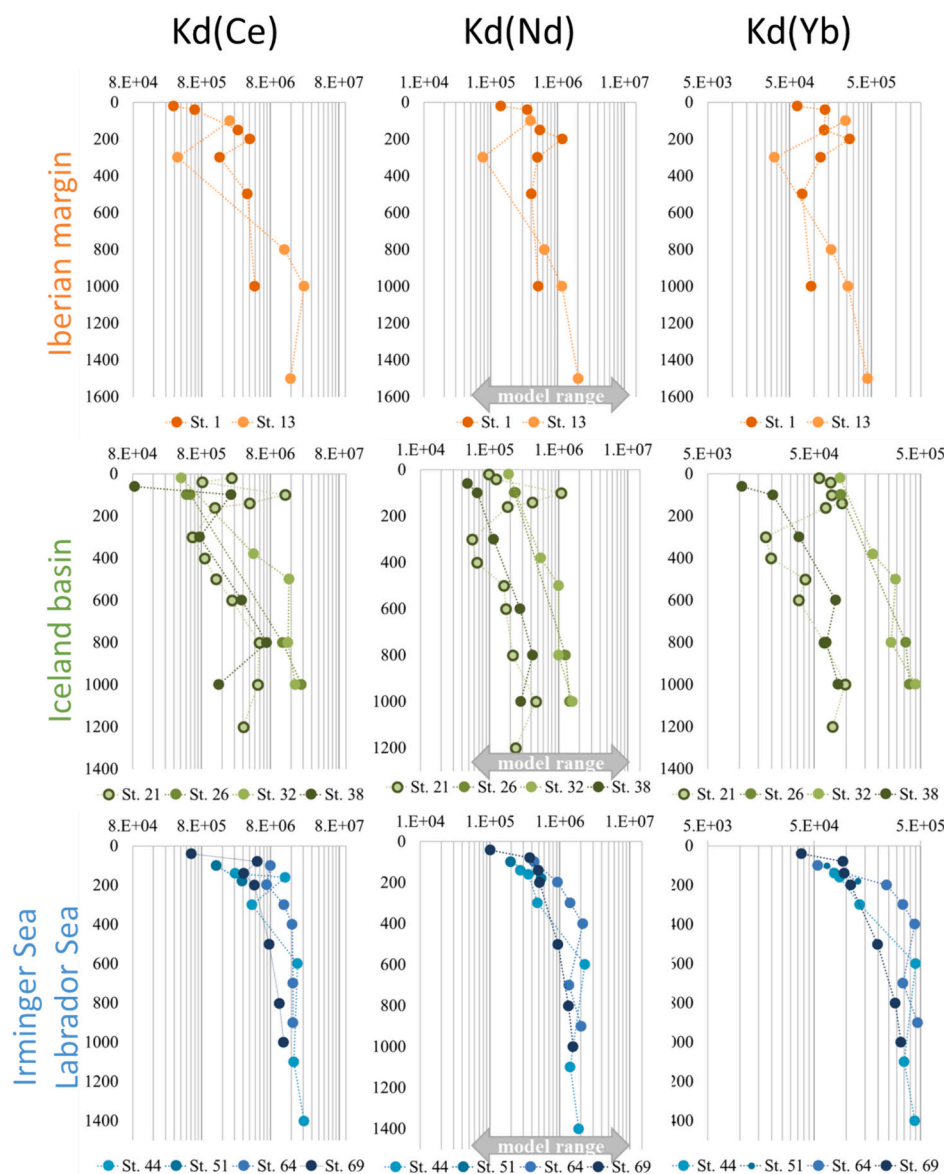
Fig. 4. Partition coefficients Kd of Ce (left column), Nd (middle column) and Yb (right column) calculated for stations close to Iberian margin (upper panels), in the Iceland basin (middle panels), in the Irminger and Labrador seas (bottom panels). The arrows on Nd profiles represent the range of Kd used to model dNd distribution in Siddall et al. (2008); Rempfer et al. (2011); Gu et al. (2017) for the different particulate phases.

these 2 stations (Fig. S2), which is remarkable given the number of parameters involved in the SPM and Kd expressions.

This whole set of data reveals that both SPM and Kd(Nd) vary broadly in the North Atlantic, with higher SPM and lower Kd(Nd) along the GEOVIDE transect compared to GA02.

The Kd(LREE) values are systematically higher than Kd(HREE) values for a same station (Fig. 4), consistent with the decreasing affinity of REE for particles along the REE series. Kd(Ce) values are the highest observed along the series, in agreement with Ce low solubility. Overall, Kd(REE) increase with depth below 400 m, and show a higher vertical variability above this depth. Kd(Nd) values fall within the wide range used in models (grey arrows in Fig. 4), whose upper limit is about one order of magnitude higher than the Kd(Nd) values measured here. Thus, Kd(Nd) could be overestimated in models mostly for POM as in the example discussed here (Arsouze et al., 2009). Throughout the various biogeochemical regions, the Kd values of all the studied REE vary within the same range ($8.6.10^4 < $ Kd(Ce) $< 2.5.10^7$, $4.3.10^4 < $ Kd(Nd) $< 2.3.10^6$; $1.10^4 < $ Kd(Yb) $< 4.7.10^5$, Fig. 4). For all REE, Kd increase more rapidly with depth in the ARCT region, and are higher there than in the

two other regions below 400 m (Kd(Nd) $> 8.10^5$ at all depth).

3.3. Partition coefficients corrected from lithogenic contribution: Kd_{authi}

As stated in the introduction, the Kd expression in eq. (4) encompasses all particulate phases, and not only the labile phase that is expected to drive particle ability to scavenge dissolved element. This issue has been underlined by Sholkovitz et al. (1994) and Tachikawa et al. (1999a). Tachikawa et al. (1999a) proposed to correct pREE concentrations from the lithogenic contribution. The corrected Kd (here referred to as Kd_{authi}) is expressed in eq. (5).

$$Kd_{authi} = \frac{[pREE] - [pREE]_{litho}}{[dREE]*SPM} \tag{5}$$

where $[pREE]_{litho}$ corresponds to REE concentration in the particulate lithogenic core. It is calculated from $p^{232}Th$ concentrations, using $(REE/^{232}Th)$ ratio in the upper continental crust, under the assumption that ^{232}Th is only lithogenic (Lagarde et al., 2020).

Kd_{authi} (of Ce, Nd and Yb) and SPM concentrations are compared to Tachikawa et al. (1999b) ones in Fig. S3. Both Kd_{authi} and SPM data compare well. The main difference is that at the mesotrophic (M) and oligotrophic (O) sites, Tachikawa et al. (1999a, 1999b) report Kd that are constant from 100 m to 2500 m (M) and 50 m to 100 m (O), the decrease in SPM concentrations being compensated by the increase in REE concentrations.

The comparison between Kd and Kd_{authi} for our set of data is presented in Fig. 5 for Nd. They display a linear relationship, varying similarly with depth, although Kd_{authi} values are roughly half of the Kd values.

Exceptions are observed at stations 1, 13, 21 (500 m), 32 (380 m) and 38 (60 m), where Kd_{authi} is ~0.2*Kd (corresponding to the lower dashed line in Fig. 5). At these locations, particles are almost entirely made of lithogenic material, i.e., quasi devoid of authigenic material (Lagarde et al., 2020). However, Lagarde et al. (2024, Part I) showed that the dissolution of a fraction of these lithogenic phases is leading to dREE enrichment. This leads us to suspect that the authigenic fraction is not the only one implicated in the particulate-dissolved reactions. Indeed, reactive lithogenic phases finding their source in dust inputs or remobilized sediments at the margins and the bottom of the ocean might also contribute to these processes. Thus, the lithogenic correction should be used carefully, after determination of the main sources of trace elements in the study area.

4. Discussion

4.1. Variations of the REE affinity for particles

In order to better describe the REE affinity for particles regardless of their abundance, Kd' (total and authigenic, this latter denominated Kd'_{authi}) were expressed as a function of SPM concentrations. Kd' was preferred to Kd as SPM is included in the Kd expression. Results are presented in Fig. 6 for Nd and in Fig. S4 for Ce and Yb.

In addition, the REE affinity variations along the section were established using the median values for Kd', Kd'_{authi} and SPM. The idea is to discuss the relative REE behavior all along the GEOVIDE section. The corresponding values are $\overline{Kd'} = 0.03$; $\overline{Kd'_{authi}} = 0.013$; and $\overline{SPM} = 90\ \mu g.kg^{-1}$; they are represented as grey dashed lines on Fig. 6. Three types of REE behaviors are identified:

- Type 1: Kd'$>\overline{Kd'}$ and SPM$<\overline{SPM}$, reflecting REE enrichment in the particulate phase compared to the section median pREE/dREE ratio, indicating a strong REE affinity for particles. The main driver of REE behavior here is particle composition. This type is shaded in purple in Fig. 6 (top left);
- Type 2: Kd'$>\overline{Kd'}$ and SPM$>\overline{SPM}$ or Kd'$<\overline{Kd'}$ and SPM$<\overline{SPM}$, representing a behavior that depends on the SPM concentrations. Kd'

and SPM vary similarly, meaning that an increase in particle concentration results in an increase in Kd', which is expected if the scavenging rate is constant. This type is shaded in blue on Fig. 6 (bottom left and top right);
- Type 3: Kd'$<\overline{Kd'}$ and SPM$>\overline{SPM}$, indicating a lower REE affinity for particles compared to the section median. This type is shaded in orange on Fig. 6 (bottom right). As for type 1, it corresponds to a behavior that depends on particle composition, but with an opposite effect on REE affinity for particles.

For Kd', type 1 encompasses station 13 below 800 m, station 51 at 180 m and most of the data points at stations 64 and 69 (Fig. 6, top panels). Regarding Kd'_{authi} (Fig. 6, bottom panels), type 1 is only found in the arctic regions. This region also corresponds to the area with the highest (hydr)oxides proportion in particles (Fig. S1). These results underline that the MnO_2 and $Fe(OH)_3$ phases are the main drivers of REE scavenging along the GEOVIDE section, confirming previous observations (Tachikawa et al., 1999b; Bau, 1999; Bau et al., 1996; Palmer and Elderfield, 1986; Ohta and Kawabe, 2001). However, their efficiency to scavenge REE seems more linked to their relative proportions in the particle pool than to their absolute concentrations. This was also observed by Lagarde et al. (2020) when comparing particulate REE, MnO_2 and $Fe(OH)_3$ concentrations. In other words, the absolute concentration of the oxides and hydroxides is likely not the best indicator of the ability of the particles to react with dREE. Instead, an increase in the MnO_2 and $Fe(OH)_3$ proportions below 800 m close to the Iberian margin and in the Iceland basin could explain the intense REE scavenging reported in Lagarde et al. (submitted, Part 1) in this area. The presence of the Arctic region in type 1 could also reflect the enhanced affinity of REE for particles containing BSi, despite its lower efficiency than Mn and Fe oxides for particle scavenging. This result supports the hypothesis that silica and REE cycles are linked to some extent (Akagi, 2013).

At stations 1, 26, 32, 38 below 600 m and at station 44, Kd'$>\overline{Kd'}$ and SPM$>\overline{SPM}$ or Kd'$<\overline{Kd'}$ and SPM$<\overline{SPM}$, what includes them in Type 2 (in blue on Fig. 6). A few points of stations 21 also fall in this type. It represents the mean REE behavior along the section. If the lithogenic correction is considered (if $Kd'_{authi}>\overline{Kd'_{authi}}$), type 2 includes the points of station 13 at 300 m, and station 38 from 100 to 1000 m, in addition to the aforementioned stations.

The data points included in type 3 for Kd' are the surface of station 1, station 21, station 38 from the surface to 300 m, and the surface of station 69. Regarding Kd'_{authi}, type 3 additionally includes points from station 1 down to 300 m. These points correspond to the area with the highest proportion of POM along the section, and for station 38 the highest proportion of $CaCO_3$. These results support the previous conclusions of an attenuation of REE affinity for particles mostly composed of organic matter and $CaCO_3$, even though it has been shown that they can scavenge REE (Palmer, 1985; Zoll and Schijf, 2012).
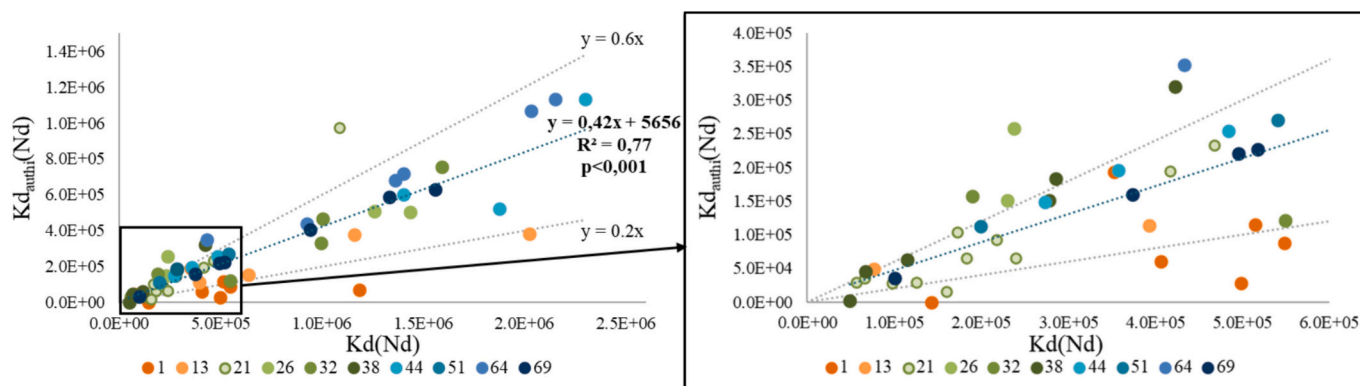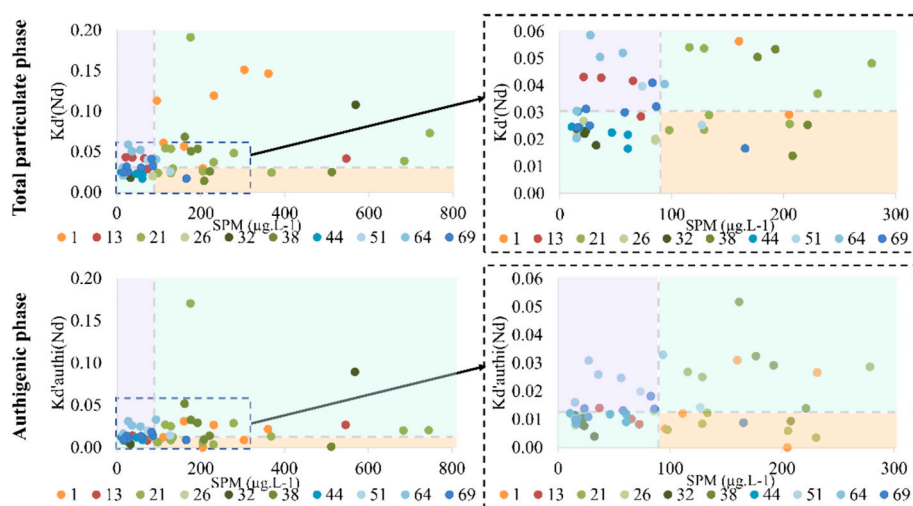

Fig. 5. Relationship between Kd(Nd) and Kd_{authi}(Nd) at the GEOVIDE stations.

Fig. 6. Neodymium particulate-to-dissolved concentration ratios in the total particulate phase (upper panels) and in the authigenic particulate phase alone (lower panels), as a function of suspended particulate matter concentration (SPM). The right panels are a zoom on the dotted square on the left. The dashed grey lines represent Kd', Kd'$_{authi}$ and SPM medians. SPM, Kd' (upper panels) and Kd'$_{authi}$ (lower panels) medians are used to delimit the different background colors, which highlight the three different types of REE affinity for particles along the GEOVIDE section: in purple, strong REE affinity for limited particles; in blue the general averaged behavior; and in orange lower REE affinity for abundant particles. (For interpretation of the references to colour in this figure legend, the reader is referred to the web version of this article.)

To conclude, REE scavenging along the GEOVIDE transect appears to be enhanced by the occurrence of MnO_2 and $Fe(OH)_3$, possibly by BSi, and weakened by POM and $CaCO_3$. This link between dREE and various particulate phases was investigated further using a Pearson correlation test.

4.2. Particle phases driving REE scavenging

In order to quantify the relative impact of the various phases composing the particles on REE scavenging, Pearson correlation tests were performed on the Kd data set using XLSTAT (Addinsoft, 2022) for three REE (Ce, Nd, Yb). For each of the REE, four Pearson correlation tests were carried out: Kd versus particulate phase concentration; Kd versus particulate phase fractions; Kd$_{authi}$ versus particulate phase concentration; Kd$_{authi}$ versus particulate phase fractions.

The coefficient values for each test, associated with their lower and upper limit in the 95% confidence interval, are shown in Fig. 7. Matrix of correlation between Kd and the proportions of the different particulate phases, with the associated confidence intervals (95%), are reported in Table S3, S4 and S5 for Nd, Ce and Yb respectively.

The Pearson correlation matrix confirms that the phases significantly correlated with Kd(REE) are the lithogenic, MnO_2 and $Fe(OH)_3$ phases (on the right in Fig. 7). For these three phases, the Pearson correlation coefficients are significantly higher between Kd (and Kd$_{authi}$) and the particulate phase fractions (in %) than between Kd (and Kd$_{authi}$) and the particulate phase concentrations (in $\mu g.kg^{-1}$). A hypothesis is that this could reflect a supply and demand issue: a larger fraction of oxides and hydroxides at the surface of the particles could decrease the competition between the various molecules for the scavenging sites.

The lithogenic fraction displays the highest correlation with Kd
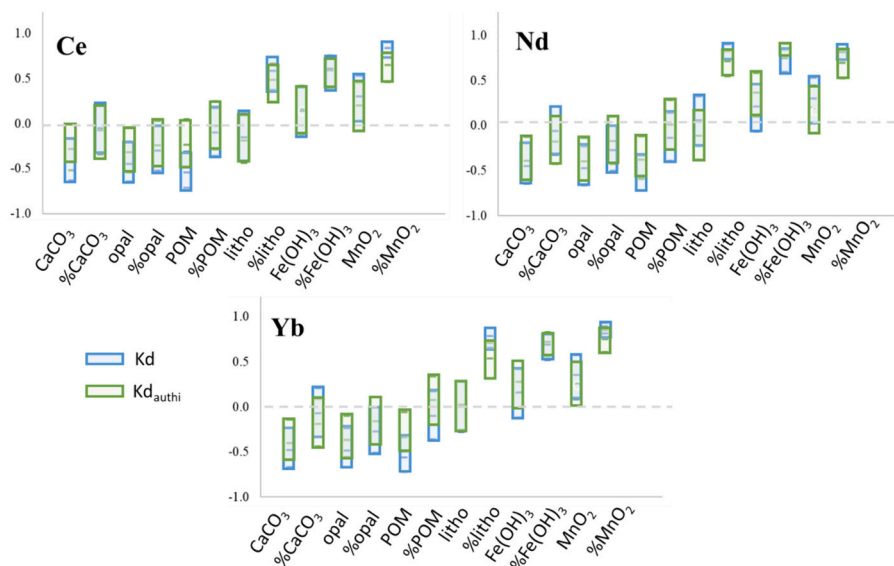
Fig. 7. Cerium, neodymium and ytterbium Pearson correlation coefficients between Kd (in blue) and Kd$_{authi}$ (in green) and the particulate phase concentrations and fractions. The colored bars delimit the 95% confidence interval of the coefficients. (For interpretation of the references to colour in this figure legend, the reader is referred to the web version of this article.)

(LREE) except for Ce, and the second most important with Kd(HREE). Kd_{authi} is also significantly correlated to the lithogenic fraction, as observed by Stichel et al. (2020). This strong influence of the lithogenic fraction can be explained by a combination of the large lithogenic inputs from margins surrounding the GEOVIDE area (Gourain et al., 2019; Lagarde et al., 2020), and the significant exchanges observed between the lithogenic and dissolved phases (Lagarde et al., 2024, Part I). It underlines the need to take this fraction into account when modeling the trace metal oceanic fate.

The strongest correlation for HREE and the second most important correlation for LREE is observed between Kd and MnO_2, confirming again that manganese oxides are the main REE carriers along the GEOVIDE section. This is even more pronounced for Ce, whose cycle is closely linked to Mn oxides (Moffett, 1990, 1994; Koeppenkastrop and De Carlo, 1992; De Carlo et al., 1997; Ohta and Kawabe, 2001). As a whole, the REE correlation with the $Fe(OH)_3$ fraction tends to be lower than with MnO_2 fraction, contradicting previous studies (Bau, 1999; Kuss et al., 2001; Koeppenkastrop and De Carlo, 1992, 1993). This discrepancy illustrates the complexity to extrapolate lab experiment results to natural environments, and the need for a more Kd, MnO_2 and $Fe(OH)_3$ data in various oceanic regions to confirm or not this tendency.

Unfortunately, our present data set is too limited to allow attributing a differential affinity for opal between HREE and LREE. It would require more samples at the surface and subsurface in both the arctic region and the Iceland basin to perform a statistical comparison.

The major role of oxides and hydroxides is not considered yet in Nd or REE cycle models (Siddall et al., 2008; Arsouze et al., 2009; Oka et al., 2009, 2021; Rempfer et al., 2011; Gu et al., 2017), which appears to be a significant limitation in the Nd cycle representation. The present work strongly suggests that adding these phases in future model developments would be a major improvement. A first approach of Kd parameterization including these two phases is proposed in the following section.

4.3. Kd(REE) parameterization based on particle composition

In this section we aimed to test the possibility to express Kd(Nd) as a function of the proportions of the different particulate fractions, which appear to be the main control on Kd values in the previous section. Having the possibility to calculate Kd(Nd) by knowing the particle composition would be of a great help, as it can be extrapolated to any particle field in the ocean without regard to export, and allows going beyond a local application. Although, it should be used with caution, as it is established from a limited area of the global ocean.

The Kd(Nd) expression as a function of the particulate phase fractions was established by linear regression using XLSTAT (Addinsoft, 2022), following Hayes et al. (2015) and Basak et al. (2024). The observed Kd(Nd) was defined as the output, and the proportions of the different phases as the explicative variables in input. Two regressions were performed: one including MnO_2 and $Fe(OH)_3$ in the particulate fractions (eq. 4), and one without (eq. 5). We limited the linear regression to Nd only, as it is the only REE modeled so far.

$$Kd(Nd) = a_1^* \%Litho + a_2^* \%Opal + a_3^* \%POM + a_4^* \%CaCO_3 + a_5^* \%Fe(OH)_3 + a_6^* \%MNO_2 \quad (6)$$

$$Kd(Nd) = a_1^* \%Litho + a_2^* \%Opal + a_3^* \%POM + a_4^* \%CaCO_3 \quad (7)$$

The resulting coefficients (a_i) and the associated errors are presented in Table 1 for the regression including oxides and hydroxides, and in Table 2 for the one without. Fig. 8 presents Kd(Nd) predicted from Eqs. (6) and (7) as a function of the observed Kd(Nd).

The predicted data display better agreement with the observed data for the parameterization including (hydr)oxides ($R^2 = 0.84$ versus $R^2 = 0.71$, Fig. 8). In this parameterization, the highest coefficients are associated with the least abundant phases that scavenge REE (MnO_2, Fe $(OH)_3$ and the lithogenic fraction), with a strong predominance of Mn

Table 1
Coefficient values associated with the six particulate phases used to determine Kd(Nd) with the associated errors and coefficient limits within a 95% confidence interval.

Parameter	Coefficient	Value	Standard error	Lower limit (95%)	Upper limit (95%)
%Litho	a_1	76,443	17,229	41,782	111,104
%Opal	a_2	−30	7214	−14,543	14,483
%POM	a_3	1344	1264	−1200	3887
%CaCO$_3$	a_4	1935	1724	−1533	5403
%Fe(OH)$_3$	a_5	438,686	286,430	−137,538	1,014,909
%MnO$_2$	a_6	11,643,995	2,105,985	7,407,300	15,880,690

Table 2
Coefficient values associated with the four particulate phases considered for Kd (Nd) calculation with the associated errors and coefficient limits within a 95% confidence interval.

Parameter	Coefficient	Value	Standard error	Lower limit (95%)	Upper limit (95%)
%LITHO	a_1	149,562	13,415	122,604	176,520
%OPAL	a_2	−8524	9390	−27,393	10,345
%POM	a_3	2728	1652	−592	6049
%CaCO3	a_4	2554	2226	−1920	7027

oxides (Table 1), which coefficient is two to four orders of magnitude higher than the other coefficients. The $Fe(OH)_3$ phase, in similar proportions as MnO_2, contributes significantly less to Kd, reflecting a lower scavenging efficiency. The large error associated with the opal coefficient prevents its comparison with the POM and $CaCO_3$ coefficients. When (hydr)oxides are not considered in the parameterization, the lithogenic fraction has the greatest impact on Kd(Nd). Phytoplanktonic tests and organic matter, however, are not efficient REE scavengers. The associated errors depend on the data set size, and more Kd(Nd) data are needed to better constrain this parameter.

Following the same approach, Basak et al. (2024) established Kd(Nd) coefficients for each of the six major particulate phases along a zonal transect in the eastern Pacific crossing the East Pacific Rise (GEO-TRACES cruise GP16). These coefficients were established for samples both within and outside a hydrothermal plume (their Table 1). Co-efficients of that study are significantly higher than those we report here, except for the lithogenic fraction (Table 3). Variability among their coefficients is of 2 orders of magnitude, which is more restrained than for our dataset (i.e., 4 orders of magnitude regardless of opal). In other words, all particulate phases along this Pacific transect contribute more equally to scavenge Nd, unlike in our North Atlantic data. Therefore, the relative role of the different particulate phases varies greatly from one oceanic region to another. It underlines the urgent need of more particulate and partition coefficient data through the global ocean to better constrain REE cycle. Like in our study, and even though their coefficient dispersion is lower, both (hydro)oxide phases remain the most important coefficients (Table 3), with the MnO_2 coefficient being higher than the $Fe(OH)_3$ one within the.

plume (no clear conclusion outside of the plume due to large error bars, their Table 1). These results confirm the major role of oxides and hydroxides in REE scavenging.

In models, Kd is parametrized for each of the particulate major constituents (Kd_{litho}, Kd_{POM}, Kd_{CaCO3}, Kd_{opal}) (Siddall et al., 2008; Arsouze et al., 2009; Ayache et al., 2023). The resulting values vary greatly from a study to another (Table 3), especially for the POM, because they depend on the particle field parametrization. The coefficients established from the linear regression are the relative Kd_X corresponding to each particulate phase: if a particle made of only one phase is considered, its corresponding coefficient is multiplied by 1 (100%) when other coefficients are multiplied by zero. These calculated
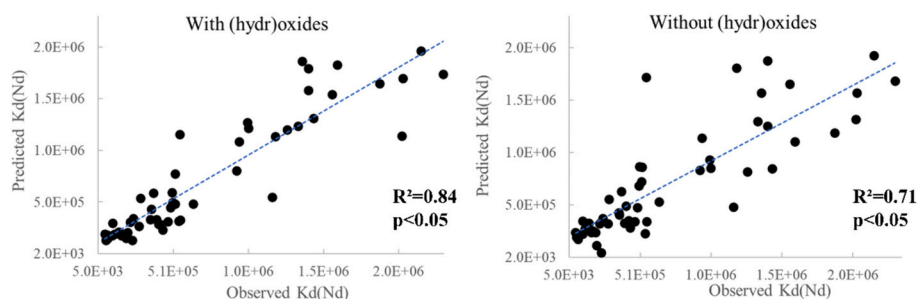
Fig. 8. Comparison between observed and predicted Kd(Nd) and the associated determination coefficient, for a parameterization considering MnO_2 and $Fe(OH)_3$ (left panel) or not (right panel). The predicted Kd(Nd) were calculated following Eqs. (6) and (7) using coefficients in Tables 1 and 2 for the left and right panels respectively.

Table 3

Comparison of Kd(Nd) in Nd cycle models, in Basak et al. (2024) study and this study. Arsouze et al. (2009) distinguished two classes of particles for organic matter, (s) small and (b) large. An * denotes coefficients established in this study presenting large errors (Table 2). In models, Kd are applied to particle phase concentrations, whereas they are applied to particulate fractions in this study.

	Kd(Nd)	Kd_{litho}	Kd_{POM}	Kd_{CaCO3}	Kd_{opal}	Kd_{MnO2}	$Kd_{Fe(OH)3}$
Siddall et al. (2008) *concentrations*	$1.1.10^5$	$2.9.10^6$	0	$2.1.10^5$	6.10^5		
Arsouze et al. (2009) *concentrations*		$4.6.10^5$	$1.4.10^7$ (s) $5.2.10^4$ (b)	$1.6.10^5$	$3.6.10^4$		
Gu et al. (2017) *concentrations*		$7.5.10^5$	$3.5.10^5$	$9.7.10^4$	$1.1.10^5$		
Oka et al. (2021) *SPM*	8.10^5						
Basak et al. (2024) **near field/far field plume** *fractions*	$\sim8.10^5$–3.10^7	$1.3.10^6$/ –	–/6.10^6	$8.3.10^6$/ $5.6.10^6$	$1.1.10^7$/ –	$2.3.10^8$/ $2.6.10^7$	$1.3.10^7$/ $4.8.10^7$
This study with (hydr)oxides *fractions*	$4.9.10^4$–$2.3.10^6$	$7.6.10^4$	$1.3.10^3$	$1.9.10^3$	-3.10^1	$1.2.10^7$	$4.4.10^5$
This study without (hydr)oxides *fractions*		$1.5.10^5$	$2.7.10^3$	$2.5.10^3$	$-8.0.10^3$		

Kd_{litho}, Kd_{POM}, Kd_{CaCO3}, Kd_{opal}, Kd_{MnO2} and $Kd_{Fe(OH)3}$ are compared to those set in different models in Table 3.

In the models, the partition coefficients attributed to POM, $CaCO_3$, and opal are overestimated to compensate for the absence of oxides and hydroxides. Siddall et al. (2008) excluded POM in the Kd(Nd) expression, thus improving the fit between modeled and observed Nd concentrations and isotopic compositions. The modeled Kd_{litho} is also overestimated, but to a lesser extent, as the lithogenic fraction becomes the main phase driving REE exchanges between the dissolved and particulate phases when (hydr)oxides are not considered. It should be noted that the Kd tuning in models is highly dependent on the generated particle field, and thus on the particulate sources such as sediment, that are associated to a great uncertainty (Siddall et al., 2008; Arsouze et al., 2009; Pasquier et al., 2022).

These results reinforce the need to include oxides and hydroxides into models to constrain the Nd cycle. Their omission leads to a defective representation of Nd exchanges between the dissolved and particulate phases, leading to a deviation between observed and modeled profiles of Nd concentration and isotopic composition. However, the results shown here are limited to one class of particle (suspended) and one area of the ocean, even if different biogeochemical provinces have been crossed in the framework of GEOVIDE. Arsouze et al. (2009) obtained a better fit between modeled and field data by considering Kd_{POM} for two classes of particles, and Ayache et al. (2023) showed that Kd_{POM} used at a global scale by Arsouze et al. (2009) and Gu et al. (2017) do not apply to the Mediterranean Sea. To progress on these issues, a strong recommendation is to produce more particulate field data (in composition and concentration). Such data will allow improving the understanding of trace metal biogeochemical cycles through observation and modeling.

5. Conclusion

This study presents the first basin scale section of REE partition coefficients (Kd) and dissolved to particulate concentration ratios (Kd'), from the surface to 1500 m, along the GEOVIDE transect (GEOTRACES GA01, May–June 2014, R/V Pourquoi Pas?). To calculate Kd, the suspended particulate matter (SPM) concentrations were estimated by using the concentrations of the various phases constituting the particulate phase (particulate organic matter, calcium carbonate, opal, lithogenic material, Mn oxides and Fe hydroxides), as well as the particulate and dissolved REE concentrations from Lagarde et al. (2020) and Lagarde et al. (2024, Part I). Kd vertical profiles displayed minimum values at the surface, non-linear variations down to 400 m, and an increase with depth below 400 m.

Particulate to dissolved concentration ratios Kd' (pREE/dREE) compared to Kd values highlighted that the pREE/dREE ratio were barely representative of the REE affinity for particles, at least close to the margins where strong lithogenic inputs occur, and at the surface where organic matter is produced. In these areas, the observed high ratios resulted from high particle concentrations. They do not reflect a higher ability of particles to scavenge REE.

The comparison between Kd' and SPM revealed that REE have a stronger affinity for particles in areas where MnO_2 and $Fe(OH)_3$ particulate proportions were the highest. Large proportions of organic matter resulted in a lower affinity for particles. This study clearly assesses that MnO_2 is the principal actor of REE scavenging in the ocean, for all REE. $Fe(OH)_3$ appears to be the second most important scavenging phase for all REE except Ce. Rather than their absolute concentrations, the relative proportions of these phases are the deciding factor in REE scavenging.

Finally, a Kd parameterization as a function of the fractions of the particulate phases showed a good agreement between observed and predicted Kd values. In this parameterization, the highest contributions to the Kd values were from MnO_2, $Fe(OH)_3$ and the lithogenic fraction. The organic matter, calcium carbonate and opal contributions to Kd were comparatively limited.

The present data set could be used in future modeling of the Nd and REE cycles. We indeed showed that the Kd values parameterized in current models are lower than those calculated in this study. We advocate that, among future model developments, MnO_2 and $Fe(OH)_3$

abundances in particles should be considered to better constrain REE scavenging by particles. A Kd parameterization using only organic matter, calcium carbonate, opal and dust concentrations, as currently done, does not correctly represent Kd.

Although we generated the largest data set ever produced, increasing the Kd data set is urgently needed to better constrain the REE cycle models. For example, the potential link between HREE and silica could not be explored from this data set and remains elusive. Furthermore, the absence of data at depth prevents investigating the effects of particle composition on reversible scavenging.

Financial support

CRediT authorship contribution statement

Marion Lagarde: Writing – original draft, Visualization, Validation, Methodology, Investigation, Formal analysis. **Viet Quoc Pham:** Writing – review & editing, Methodology. **Nolwenn Lemaitre:** Writing – review & editing, Methodology. **Moustafa Belhadj:** Resources, Methodology. **Catherine Jeandel:** Writing – review & editing, Validation, Supervision, Resources, Project administration, Methodology, Investigation, Funding acquisition, Conceptualization.

Declaration of competing interest

The authors declare that they have no known competing financial interests or personal relationships that could have appeared to influence the work reported in this paper.

Data availability

All data are included in the supplement

Acknowledgements

Appendix A. Supplementary data

Supplementary data to this article can be found online at https://doi.org/10.1016/j.chemgeo.2024.122298.

References

Addinsoft, 2022. XLSTAT Statistical and Data Analysis Solution.

Akagi, T., 2013. Rare earth element (REE)–silicic acid complexes in seawater to explain the incorporation of REEs in opal and the "leftover" REEs in surface water: New interpretation of dissolved REE distribution profiles. Geochim. Cosmochim. Acta 113, 174–192.

Akagi, T., Fu, F., Hongo, Y., Takahashi, K., 2011. Composition of rare earth elements in settling particles collected in the highly productive North Pacific Ocean and Bering Sea: Implications for siliceous-matter dissolution kinetics and formation of two REE-enriched phases. Geochim. Cosmochim. Acta 75, 4857–4876.

Anderson, R.F., 2003. 6.09 - Chemical tracers of particle transport. In: Holland, H.D., Turekian, K.K. (Eds.), Treatise on Geochemistry. Pergamon, Oxford, pp. 247–273.

Anderson, R.F., Henderson, G.M., 2015. A Global Study of the Marine Biogeochemical, 18, pp. 76–79.

Anderson, R.F., Bacon, M.P., Brewer, P.G., 1983. Removal of 230Th and 231Pa at ocean margins. Earth Planet. Sci. Lett. 66, 73–90.

Arsouze, T., Dutay, J.-C., Lacan, F., Jeandel, C., 2009. Reconstructing the Nd oceanic cycle using a coupled dynamical – biogeochemical model. Biogeosciences 6, 2829–2846.

Ayache, M., Dutay, J.-C., Tachikawa, K., Arsouze, T., Jeandel, C., 2023. Neodymium budget in the Mediterranean Sea: evaluating the role of atmospheric dusts using a high-resolution dynamical-biogeochemical model. Biogeosciences 20, 205–227.

Basak, C., Wu, Y., Haley, B.A., Muratli, J., Pena, L.D., Bolge, L., Fitzsimmons, J.N., Sherrell, R.M., Goldstein, S.L., 2024. Suspended particulate matter influence on dissolved Nd concentration and isotopic composition along GEOTRACES section GP16. Earth Planet. Sci. Lett. 635, 118692.

Bau, M., 1999. Scavenging of dissolved yttrium and rare earths by precipitating iron oxyhydroxide: Experimental evidence for Ce oxidation, Y-Ho fractionation, and lanthanide tetrad effect. Geochim. Cosmochim. Acta 63, 67–77.

Bau, M., Dulski, P., 1996. Distribution of yttrium and rare-earth elements in the Penge and Kuruman iron-formations, Transvaal Supergroup, South Africa. Precambrian Res. 79, 37–55.

Bau, M., Koschinsky, A., 2009. Oxidative scavenging of cerium on hydrous Fe oxide: evidence from the distribution of rare earth elements and yttrium between Fe oxides and Mn oxides in hydrogenetic ferromanganese crusts. Geochem. J. 43, 37–47.

Bau, M., Koschinsky, A., Dulski, P., Hein, J.R., 1996. Comparison of the partitioning behaviours of yttrium, rare earth elements, and titanium between hydrogenetic marine ferromanganese crusts and seawater. Geochim. Cosmochim. Acta 60, 1709–1725.

Bayon, G., Lemaitre, N., Barrat, J.-A., Wang, X., Feng, D., Duperron, S., 2020. Microbial utilization of rare earth elements at cold seeps related to aerobic methane oxidation. Chem. Geol. 555, 119832.

Boyd, P.W., Jickells, T., Law, C.S., Blain, S., Boyle, E.A., Buesseler, K.O., Coale, K.H., Cullen, J.J., Baar, H.J.W., de Follows, M., Harvey, M., Lancelot, C., Levasseur, M., Owens, N.P.J., Pollard, R., Rivkin, R.B., Sarmiento, J., Schoemann, V., Smetacek, V., Takeda, S., Tsuda, A., Turner, S., Watson, A.J., 2007. Mesoscale Iron Enrichment experiments 1993-2005: Synthesis and Future Directions. Science 315, 612–617.

Bruland, K.W., Lohan, M.C., 2003. 6.02 - Controls of trace metals in seawater. In: Holland, H.D., Turekian, K.K. (Eds.), Treatise on Geochemistry. Pergamon, Oxford, pp. 23–47.

Bruland, K.W., Lohan, M.C., 2006. 6.02 Controls of Trace Metals in Seawater, 25.

Burnett, W.C., Dulaiova, H., Stringer, C., Peterson, R., 2006. Submarine groundwater discharge: its measurement and influence on the Coastal Zone. J. Coast. Res. 4.

Byrne, R.H., Kim, K.-H., 1990. Rare earth element scavenging in seawater. Geochim. Cosmochim. Acta 54, 2645–2656.

Chase, Z., Anderson, R.F., Fleisher, M.Q., Kubik, P.W., 2002. The influence of particle composition and particle flux on scavenging of Th, Pa and be in the ocean. Earth Planet. Sci. Lett. 204, 215–229.

de Baar, H.J.W., Boyd, P.W., Coale, K.H., Landry, M.R., Tsuda, A., Assmy, P., Bakker, D. C.E., Bozec, Y., Barber, R.T., Brzezinski, M.A., Buesseler, K.O., Boyé, M., Croot, P.L., Gervais, F., Gorbunov, M.Y., Harrison, P.J., Hiscock, W.T., Laan, P., Lancelot, C., Law, C.S., Levasseur, M., Marchetti, A., Millero, F.J., Nishioka, J., Nojiri, Y., van Oijen, T., Riebesell, U., Rijkenberg, M.J.A., Saito, H., Takeda, S., Timmermans, K.R., Veldhuis, M.J.W., Waite, A.M., Wong, C.-S., 2005. Synthesis of iron fertilization experiments: from the Iron Age in the Age of Enlightenment. J. Geophys. Res. Oceans 110.

De Carlo, E.H., Wen, X.-Y., Irving, M., 1997. The Influence of Redox Reactions on the Uptake of Dissolved Ce by Suspended Fe and Mn Oxide Particles. Aquat. Geochem. 3, 357–389.

Deng, Y., Ren, J., Guo, Q., Cao, J., Wang, H., Liu, C., 2017. Rare earth element geochemistry characteristics of seawater and porewater from deep sea in western Pacific. Sci. Rep. 7, 16539.

Duce, R.A., Liss, P.S., Merrill, J.T., Atlas, E.L., Buat-Menard, P., Hicks, B.B., Miller, J.M., Prospero, J.M., Arimoto, R., Church, T.M., Ellis, W., Galloway, J.N., Hansen, L., Jickells, T.D., Knap, A.H., Reinhardt, K.H., Schneider, B., Soudine, A., Tokos, J.J., Tsunogai, S., Wollast, R., Zhou, M., 1991. The atmospheric input of trace species to the world ocean. Glob. Biogeochem. Cycles 5, 193–259.

Elderfield, H., 1988. The oceanic chemistry of the rare-earth elements. Philos. Trans. R. Soc. Lond. A 105–126.

Fonseca-Batista, D., Li, X., Riou, V., Michotey, V., Deman, F., Fripiat, F., Guasco, S., Brion, N., Lemaitre, N., Tonnard, M., Gallinari, M., Planquette, H., Planchon, F., Sarthou, G., Elskens, M., LaRoche, J., Chou, L., Dehairs, F., 2019. Evidence of high N2 fixation rates in the temperate northeast Atlantic. Biogeosciences 16, 999–1017. 10.5194/bg-16-999-2019.

García-Ibáñez, M.I., Pardo, P.C., Carracedo, L.I., Mercier, H., Lherminier, P., Ríos, A.F., Pérez, F.F., 2015. Structure, transports and transformations of the water masses in the Atlantic Subpolar Gyre. Progr. Oceanogr. 135, 18–36. https://doi.org/10.1016/j.pocean.2015.03.009.

García-Ibáñez, M.I., Pérez, F.F., Lherminier, P., Zunino, P., Mercier, H., Tréguer, P., 2018. Water mass distributions and transports for the 2014 GEOVIDE cruise in the North Atlantic. Biogeosciences 15, 2075–2090. https://doi.org/10.5194/bg-15-2075-2018.

Garcia-Solsona, E., Jeandel, Catherine, Labatut, Marie, Lacan, François, Vance, Derek, Chavagnac, Valérie, Pradoux, Catherine, 2014. Rare earth elements and Nd isotopes tracing water mass mixing and particle-seawater interactions in the SE Atlantic. Geochim. Cosmochim. Acta 125, 351–372.

Goldberg, E.D., 1954. Marine Geochemistry 1. Chemical Scavengers of the Sea. J. Geol. 62, 249–265.

Gourain, A., Planquette, H., Cheize, M., Lemaitre, N., Menzel Barraqueta, J.-L., Shelley, R., Lherminier, P., Sarthou, G., 2019. Inputs and processes affecting the distribution of particulate iron in the North Atlantic along the GEOVIDE (GEOTRACES GA01) section. Biogeosciences 16, 1563–1582.

Grenier, M., Garcia-Solsona, E., Lemaitre, N., Trull, T.W., Bouvier, V., Nonnotte, P., van Beek, P., Souhaut, M., Lacan, F., Jeandel, C., 2018. Differentiating Lithogenic Supplies, Water Mass Transport, and Biological Processes on and off the Kerguelen Plateau using rare Earth Element Concentrations and Neodymium Isotopic Compositions. Front. Mar. Sci. 5, 426.

Gu, S., Liu, Z., Jahn, A., Rempfer, J., Zhang, J., Joos, F., 2017. Neodymium isotopes in the ocean from the Community Earth System Model (CESM1.3). Geosci. Model Dev. Discuss. 2017, 1–41.

Hayes, C.T., Anderson, R.F., Fleisher, M.Q., Vivancos, S.M., Lam, P.J., Ohnemus, D.C., Huang, K.-F., Robinson, L.F., Lu, Y., Cheng, H., Edwards, R.L., Moran, S.B., 2015. Intensity of Th and Pa scavenging partitioned by particle chemistry in the North Atlantic Ocean. Mar. Chem. 170, 49–60.

Jeandel, C., Oelkers, E.H., 2015. The influence of terrigenous particulate material dissolution on ocean chemistry and global element cycles. Chem. Geol. 395, 50–66.

Jeandel, C., Bishop, J.K., Zindler, A., 1995. Exchange of neodymium and its isotopes between seawater and small and large particles in the Sargasso Sea. Geochim. Cosmochim. Acta 59, 535–547.

Jeandel, C., Thouron, D., Fieux, M., 1998. Concentrations and isotopic compositions of neodymium in the eastern Indian Ocean and Indonesian straits. Geochim. Cosmochim. Acta 62, 2597–2607.

Jeandel, C., van der Loeff, M.R., Lam, P.J., Roy-Barman, M., Sherrell, R.M., Kretschmer, Sven, German, Chris, Dehairs, Frank, 2015. What did we learn about ocean particle dynamics in the GEOSECS–JGOFS era? Prog. Oceanogr. 133, 6–16.

Jickells, T.D., Baker, A.R., Chance, R., 2016. Atmospheric transport of trace elements and nutrients to the oceans. Philos. Trans. R. Soc. A Math. Phys. Eng. Sci. 374, 20150286.

Koeppenkastrop, D., De Carlo, E.H., 1992. Sorption of rare-earth elements from seawater onto synthetic mineral particles: an experimental approach. Chem. Geol. 95, 251–263.

Koeppenkastrop, D., De Carlo, E.H., 1993. Uptake of rare earth elements from solution by metal oxides. Environ. Sci. Technol. 27, 1796–1802.

Kuss, J., Garbe-Schönberg, C.-D., Kremling, K., 2001. Rare earth elements in suspended particulate material of North Atlantic surface waters. Geochim. Cosmochim. Acta 65, 187–199.

Labatut, M., Lacan, F., Pradoux, C., Chmeleff, J., Radic, A., Murray, J.W., Poitrasson, F., Johansen, A.M., Thil, F., 2014. Iron sources and dissolved-particulate interactions in the seawater of the Western Equatorial Pacific, iron isotope perspectives. Glob. Biogeochem. Cycles 28, 1044–1065.

Lacan, F., Jeandel, C., 2001. Tracing Papua New Guinea imprint on the central Equatorial Paci¢c Ocean using neodymium isotopic compositions and rare Earth Element patterns. Earth Planet. Sci. Lett. 497–512.

Lagarde, M., Lemaitre, N., Planquette, H., Grenier, M., Belhadj, M., Lherminier, P., Jeandel, C., 2020. Particulate rare earth element behavior in the North Atlantic (GEOVIDE cruise). Biogeosciences 17, 5539–5561.

Lagarde, M., Pham, V.Q., Lherminier, P., Belhadj, M., Jeandel, C., 2024. Rare earth elements in the North Atlantic, part I: Non-conservative behavior reveals margin inputs and deep waters scavenging. Chem. Geol. 122230 https://doi.org/10.1016/j.chemgeo.2024.122230.

Lal, D., 1977. The Oceanic Microcosm of Particles, 198, p. 13.

Lam, P.J., Marchal, O., 2015. Insights into Particle Cycling from Thorium and Particle Data. Annu. Rev. Mar. Sci. 7, 159–184.

Lam, P.J., Twining, B.S., Jeandel, C., Roychoudhury, A., Resing, J.A., Santschi, P.H., Anderson, R.F., 2015. Methods for analyzing the concentration and speciation of major and trace elements in marine particles. Prog. Oceanogr. 133, 32–42.

Lemaitre, N., Planquette, H., Sarthou, G., Jacquet, S., García-Ibáñez, M.I., Gourain, A., Cheize, M., Monin, L., André, L., Laha, P., Terryn, H., Dehairs, F., 2018. Particulate barium tracing of significant mesopelagic carbon remineralisation in the North Atlantic. Biogeosciences 15, 2289–2307.

Libes, S., 2009. Introduction to Marine Biogeochemistry. Academic Press.

Longhurst, A., 1995. Seasonal cycles of pelagic production and consumption. Prog. Oceanogr. 36, 77–167. https://doi.org/10.1016/0079-6611(95)00015-1.

Marsay, C.M., Sanders, R.J., Henson, S.A., Pabortsava, K., Achterberg, E.P., Lampitt, R.S., 2015. Attenuation of sinking particulate organic carbon flux through the mesopelagic ocean. Proc. Natl. Acad. Sci. USA 112, 1089–1094. https://doi.org/10.1073/pnas.1415311112.

McCave, I.N., Hall, I.R., 2002. Turbidity of waters over the Northwest Iberian continental margin. Prog. Oceanogr. 52, 299–313. https://doi.org/10.1016/S0079-6611(02)00012-5.

Meyer, A.C.S., Grundle, D., Cullen, J.T., 2021. Selective uptake of rare earth elements in marine systems as an indicator of and control on aerobic bacterial methanotrophy. Earth Planet. Sci. Lett. 558, 116756.

Moffett, J.W., 1990. Microbially mediated cerium oxidation in sea water. Nature 345, 421–423.

Moffett, J.W., 1994. The relationship between cerium and manganese oxidation in the marine environment. Limnol. Oceanogr. 39, 1309–1318.

Moore, W.S., 1996. Large groundwater inputs to coastal waters revealed by 226Ra enrichments. Nature 380, 612–614.

Moore, C.M., Mills, M.M., Arrigo, K.R., Berman-Frank, I., Bopp, L., Boyd, P.W., Galbraith, E.D., Geider, R.J., Guieu, C., Jaccard, S.L., Jickells, T.D., La Roche, J., Lenton, T.M., Mahowald, N.M., Marañón, E., Marinov, I., Moore, J.K., Nakatsuka, T., Oschlies, A., Saito, M.A., Thingstad, T.F., Tsuda, A., Ulloa, O., 2013. Processes and patterns of oceanic nutrient limitation. Nat. Geosci. 6, 701–710.

Ohta, A., Kawabe, I., 2001. REE(III) adsorption onto Mn dioxide (ᵧ-MnO2) and Fe oxyhydroxide: Ce(III) oxidation by ᵧ-MnO2. Geochim. Cosmochim. Acta 65, 695–703.

Oka, A., Hasumi, H., Obata, H., Gamo, T., Yamanaka, Y., 2009. Study on vertical profiles of rare earth elements by using an ocean general circulation model: SIMULATION OF REES BY OGCM. Glob. Biogeochem. Cycles 23 n/a-n/a.

Oka, A., Tazoe, H., Obata, H., 2021. Simulation of global distribution of rare earth elements in the ocean using an ocean general circulation model. J. Oceanogr. 77, 413–430.

Palmer, M.R., 1985. Rare earth elements in foraminifera tests. Earth Planet. Sci. Lett. 73, 285–298.

Palmer, M.R., Elderfield, H., 1986. Rare earth elements and neodymium isotopes in ferromanganese oxide coatings of Cenozoic foraminifera from the Atlantic Ocean. Geochim. Cosmochim. Acta 50, 409–417.

Pasquier, B., Hines, S.K.V., Liang, H., Wu, Y., Goldstein, S.L., John, S.G., 2022. GNOM v1.0: an optimized steady-state model of the modern marine neodymium cycle. Geosci. Model Dev. 15, 4625–4656.

Planquette, H., Statham, P.J., Fones, G.R., Charette, M.A., Moore, C.M., Salter, I., Nédélec, F.H., Taylor, S.L., French, M., Baker, A.R., Mahowald, N., Jickells, T.D., 2007. Dissolved iron in the vicinity of the Crozet Islands, Southern Ocean. Deep Sea Res. Part II Top. Stud. Oceanogr. 54, 1999–2019.

Pollard, R., Sanders, R., Lucas, M., Statham, P., 2007. The Crozet Natural Iron Bloom and Export Experiment (CROZEX). Deep Sea Res. Part II Top. Stud. Oceanogr. 54, 1905–1914.

Pöppelmeier, F., Lippold, J., Blaser, P., Gutjahr, M., Frank, M., Stocker, T.F., 2022. Neodymium isotopes as a paleo-water mass tracer: A model-data reassessment. Quat. Sci. Rev. 279, 107404.

Rempfer, J., Stocker, T.F., Joos, F., Dutay, J.-C., Siddall, M., 2011. Modelling Nd-isotopes with a coarse resolution ocean circulation model: Sensitivities to model parameters and source/sink distributions. Geochim. Cosmochim. Acta 75, 5927–5950.

Roy-Barman, M., Jeandel, C., 2016. Marine Geochemistry: Ocean Circulation, Carbon Cycle and Climate Change. Oxford University Press, Oxford.

Roy-Barman, M., Jeandel, C., Souhaut, M., Loeff, M.R., van der, Voege I., Leblond N. and Freydier R., 2005. The influence of particle composition on thorium scavenging in the NE Atlantic ocean (POMME experiment). Earth Planet. Sci. Lett. 240, 681–693.

Roy-Barman, M., Lemaître, C., Ayrault, S., Jeandel, C., Souhaut, M., Miquel, J.-C., 2009. The influence of particle composition on Thorium scavenging in the Mediterranean Sea. Earth Planet. Sci. Lett. 286, 526–534.

Sanders, R., Henson, S.A., Koski, M., De La Rocha, C., Painter, S.C., Poulton, A.J., Riley, J., Salihoglu, B., Visser, A., Yool, A., Bellerby, R., Martin, A.P., 2014. The Biological Carbon Pump in the North Atlantic. Prog. Oceanogr. 129, 200–218. https://doi.org/10.1016/j.pocean.2014.05.005.

Sarmiento, J.L., Gruber, N., 2006. Carbon cycle. In: Ocean Biogeochemical Dynamics, pp. 318–391.

Sarthou, G., Lherminier, P., Achterberg, E.P., Alonso-Pérez, F., Bucciarelli, E., Boutorh, J., Bouvier, V., Boyle, E.A., Branellec, P., Carracedo, L.I., Casacuberta, N., Castrillejo, M., Cheize, M., Contreira, Pereira L., Cossa, D., Daniault, N., De Saint-Léger, E., Dehairs, F., Deng, F., Desprez de Gésincourt, F., Devesa, J., Foliot, L., Fonseca-Batista, D., Gallinari, M., García-Ibáñez, M.I., Gourain, A., Grosssteffan, E., Hamon, M., Heimbürger, L.E., Henderson, G.M., Jeandel, C., Kermabon, C., Lacan, F., Le Bot, P., Le Goff, M., Le Roy, E., Lefèbvre, A., Leizour, S., Lemaitre, N., Masqué, P., Ménage, O., Menzel Barraqueta, J.-L., Mercier, H., Perault, F., Pérez, F. F., Planquette, H.F., Planchon, F., Roukaerts, A., Sanial, V., Sauzède, R., Schmechtig, C., Shelley, R.U., Stewart, G., Sutton, J.N., Tang, Y., Tisnérat-Laborde, N., Tonnard, M., Tréguer, P., van Beek, P., Zurbrick, C.M., Zunino, P., 2018. Introduction to the French GEOTRACES North Atlantic Transect (GA01): GEOVIDE cruise. Biogeosciences 15, 7097–7109.

Schijf, J., Christenson, E.A., Byrne, R.H., 2015. YREE scavenging in seawater: A new look at an old model. Mar. Chem. 177, 460–471.

Schlitzer, R., 2023. Ocean Data View, https://odv.awi.de.

SCOR, 2007. GEOTRACES – An international study of the global marine biogeochemical cycles of trace elements and their isotopes. Geochemistry 67, 85–131. https://doi.org/10.1016/j.chemer.2007.02.001.

Shiller, A.M., Chan, E.W., Joung, D.J., Redmond, M.C., Kessler, J.D., 2017. Light rare earth element depletion during Deepwater Horizon blowout methanotrophy. Sci. Rep. 7, 10389.

Sholkovitz, E.R., Landing, W.M., Lewis, B.L., 1994. Ocean particle chemistry: the fractionation of rare earth elements between suspended particles and seawater. Geochim. Cosmochim. Acta 58, 1567–1579.

Sholkovitz, E.R., Elderfield, H., Szymczak, R., Casey, K., 1999. Island weathering: river sources of rare earth elements to the Western Pacific Ocean. Mar. Chem. 68, 39–57.

Siddall, M., Khatiwala, S., van de Flierdt, T., Jones, K., Goldstein, S.L., Hemming, S., Anderson, R.F., 2008. Towards explaining the Nd paradox using reversible scavenging in an ocean general circulation model. Earth Planet. Sci. Lett. 274, 448–461.

Stichel, T., Kretschmer, S., Geibert, W., Lambelet, M., Plancherel, Y., Rutgers van der Loeff, M., van de Flierdt, T., 2020. Particle–Seawater Interaction of Neodymium in the North Atlantic. ACS Earth Space Chem. 4, 1700–1717.

Sutorius, M., Mori, C., Greskowiak, J., Boettcher, L., Bunse, C., Dittmar, T., Dlugosch, L., Hintz, N.H., Simon, M., Striebel, M., Pahnke, K., 2022. Rare earth element behaviour in seawater under the influence of organic matter cycling during a phytoplankton spring bloom – A mesocosm study. Front. Mar. Sci. 9, 895723.

Tachikawa, K., Jeandel, C., Roy-Barman, M., 1999a. A new approach to the Nd residence time in the ocean: the role of atmospheric inputs. Earth Planet. Sci. Lett. 170, 433–446.

Tachikawa, K., Jeandel, C., Vangriesheim, A., Dupré, B., 1999b. Distribution of rare earth elements and neodymium isotopes in suspended particles of the tropical Atlantic Ocean (EUMELI site). Deep Sea Res. Part Oceanogr. Res. Pap. 46, 733–755.

Tagliabue, A., Buck, K.N., Sofen, L.E., Twining, B.S., Aumont, O., Boyd, P.W., Caprara, S., Homoky, W.B., Johnson, R., König, D., Ohnemus, D.C., Sohst, B., Sedwick, P., 2023. Authigenic mineral phases as a driver of the upper-ocean iron cycle. Nature 620, 104–109.

Tonnard, M., 2018. Etude du cycle biogéochimique du fer: distribution et spéciation dans l'Océan Atlantique Nord (GA01) et l'Océan Austral (GIpr05) (GEOTRACES) 412.

Turekian, K.K., 1977. The fate of metals in the oceans. Geochim. Cosmochim. Acta 41, 1139–1144.

Zoll, A.M., Schijf, J., 2012. A surface complexation model of YREE sorption on Ulva lactuca in 0.05–5.0M NaCl solutions. Geochim. Cosmochim. Acta 97, 183–199.

Zunino, P., Lherminier, P., Mercier, H., Daniault, N., García-Ibáñez, M.I., Pérez, F.F., 2017. The GEOVIDE cruise in May–June 2014 reveals an intense Meridional Overturning Circulation over a cold and fresh subpolar North Atlantic. Biogeosciences 14, 5323–5342. https://doi.org/10.5194/bg-14-5323-2017.